



# Soliton microwave oscillators using oversized billion Q optical microresonators

Lu Yao,<sup>1,2,†</sup> Peng Liu,<sup>1,3,†</sup> Hao-Jing Chen,<sup>1</sup> Qihuang Gong,<sup>1,4,5</sup> Qi-Fan Yang,<sup>1,4,6</sup> and Yun-Feng Xiao<sup>1,2,4,5,7</sup>

<sup>1</sup>State Key Lab for Mesoscopic Physics and Frontiers Science Center for Nano-optoelectronics, School of Physics, Peking University, Beijing, 100871, China

<sup>2</sup>National Biomedical Imaging Center, Peking University, 100871, Beijing, China

<sup>3</sup>School of Electronics Engineering and Computer Science, Peking University, Beijing, 100871, China

<sup>4</sup>Collaborative Innovation Center of Extreme Optics, Shanxi University, 030006, Taiyuan, China

<sup>5</sup>Peking University Yangtze Delta Institute of Optoelectronics, Nantong, Jiangsu 226010, China

<sup>6</sup>e-mail: leonardoyoung@pku.edu.cn

<sup>7</sup>e-mail: yfxiao@pku.edu.cn

Received 22 March 2022; revised 30 April 2022; accepted 30 April 2022; published 16 May 2022

**Microresonator soliton frequency combs offer unique flexibility in synthesizing microwaves over a wide range of frequencies, while their phase noise is currently limited by thermal noise. Enlarging the mode volume would mitigate thermal noise but also raise power consumption. Here, we fabricate optical microresonators with large mode volumes by lathe machining high-purity fiber preforms. Quality factors greater than 4 billion result in a record-low threshold power of 110  $\mu\text{W}$  to initiate comb operation in millimeter-sized devices. The synthesized X-band microwaves with an absolute phase noise level of  $-107(-133)$  dBc/Hz at 1(10) kHz offset frequency feature considerable noise reduction compared to other silica-microresonator-based oscillators, which are further used to cope with high-speed data links as carrier waves. Our work illuminates a pathway toward low-noise photonic microwave generation as well as the quantum regime of soliton microcombs.** © 2022 Optica Publishing Group under the terms of the Optica Open Access Publishing Agreement

<https://doi.org/10.1364/OPTICA.459130>

Optical microresonators have emerged as powerful engines in the microwave world [1]. By virtue of high quality ( $Q$ ) factors, they have been adopted in optoelectronic oscillators as narrow-linewidth optical filters [2]. On the other hand, microresonators are also able to function as standalone microwave oscillators if nonlinear optical properties are explored [3,4]. In particular, microresonator-based optical frequency combs operated in the soliton regime (“soliton microcombs”) provide a compelling approach to synthesize microwaves in compact form factors [5–15]. The optical-to-microwave conversion is realized by photodetecting the repetitive soliton pulse train that emits from the microresonator at a rate determined by its free spectral range (FSR). In contrast to the narrow bandwidth of Brillouin oscillators [3,16,17], these soliton microwave oscillators (SMOs) offer extreme frequency flexibility from gigahertz [9] to terahertz [10], which is attributed to the broadband Kerr parametric gain.

Nevertheless, frequencies below microwave X-bands (<12 GHz) are difficult to access in these devices, since the required large cavity size will result in a high pump power to sustain the comb operation. Currently, microresonators made of silica [8,18], MgF<sub>2</sub> [7,12], and Si<sub>3</sub>N<sub>4</sub> [11] are exclusive platforms to allow microcomb operation in this realm.

The coherence of the synthesized microwaves is the key performance driver for a plurality of applications. For instance, the utmost data rates of a wireless communications channel would benefit from the leveraged spectral purity of the carrier microwave [19]. It has been demonstrated that noise inherited from the pump laser can be effectively suppressed by operating the microcomb near a so-called “quiet point” [11,12,20,21]. In this way, noise having more fundamental origins are revealed, especially thermal noise that couples to the SMO in various pathways [21,22]. According to thermodynamics, mitigated thermal noise is anticipated in the mode spanning a larger volume and equivalently a larger mode area for a given FSR [21,23–26]. However, this approach causes a significant drawback in power efficiency due to the aforementioned power scaling.

In this Letter, we resolve such tension by simultaneously boosting the  $Q$  factors and mode areas of optical microresonators. High-purity silica fiber preforms are lathe machined to form microresonators with spherical peripheries for large mode volumes [27]. In microresonators with diameters of 6 mm, a quality factor exceeding 4 billion is demonstrated. The resulting parametric oscillation threshold of 112  $\mu\text{W}$  is a record low among documented millimeter-sized devices [11,28]. The phase noise of the generated 11 GHz SMO reaches  $-107$  dBc/Hz and  $-133$  dBc/Hz at 1 kHz and 10 kHz offset frequencies, respectively, showing a 10 dB improvement compared to other free-running oscillators based on silica microresonators. To further bench the performance of the SMO, its implementation as the local oscillator in a data transmitter to support 256 and 1024 quadrature amplitude modulation (QAM) is also demonstrated for the first time, to the best of our knowledge.

Whispering-gallery-mode microresonators with spherical cross sections can easily access large mode areas, since the confinement

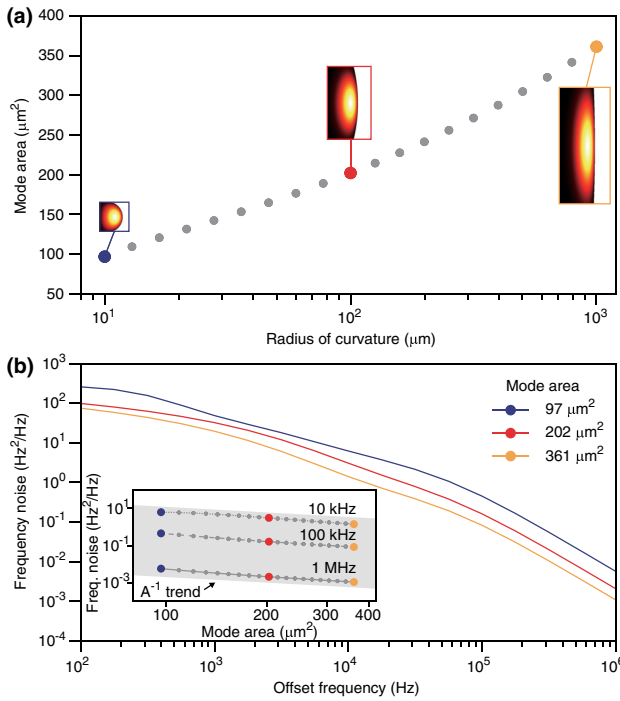


**Fig. 1.** Mode area and thermorefractive noise. (a) Simulated effective mode area of the fundamental TM mode versus radius of curvature of the microresonator. Representative modal profiles are also plotted at the same scale. (b) Simulated single-sideband (SSB) thermorefractive noise of the resonant frequencies of three modes with different effective mode area [indicated by colors in accordance with (a)]. Inset: Simulated thermorefractive noise versus effective mode area at 10 kHz, 100 kHz, and 1 MHz offset frequencies. Parameters used in the simulation are:  $n_0 = 1.45$ ,  $n_T = 1.1 \times 10^{-5} \text{ K}^{-1}$ ,  $\rho = 2203 \text{ kg m}^{-3}$ ,  $C = 703 \text{ J kg}^{-1} \text{ K}^{-1}$ , and  $k = 1.38 \text{ W m}^{-1} \text{ K}^{-1}$ .

in the vertical direction is relaxed compared to microresonators with wedged [28,29], ridged [18], belt [30], or toroidal [31] shapes. Using the finite-element-method, the effective mode area is computed for a silica microresonator with respect to the radius of curvature of its cross-sectional periphery. As shown in Fig. 1(a), the effective mode area of the fundamental transverse magnetic (TM) mode expands as the radius of curvature increases. The thermal noise associated with these modes is evaluated in terms of the noise of their resonant frequencies [24,32], which scale as

$$S_T \sim \frac{n_T^2 k_B T^2 D_1}{n_0^2 \rho C A}. \quad (1)$$

Here,  $n_T$  and  $n_0$  are, respectively, the thermo-optic coefficient and linear refractive index of the material;  $k_B$  is the Boltzmann constant;  $T$  is the temperature; and  $\rho$ ,  $C$ ,  $D_1$ , and  $A$  represent, respectively, the mass density, specific heat, FSR, and the mode area. The power spectral density of such thermorefractive noise is further simulated based on the fluctuation-dissipation theorem [24]. The results plotted in Fig. 1(b) manifest the negative correlation between such thermorefractive noise (TRN) and the effective mode area  $A$ , approximately following an  $A^{-1}$  trend [24,32].

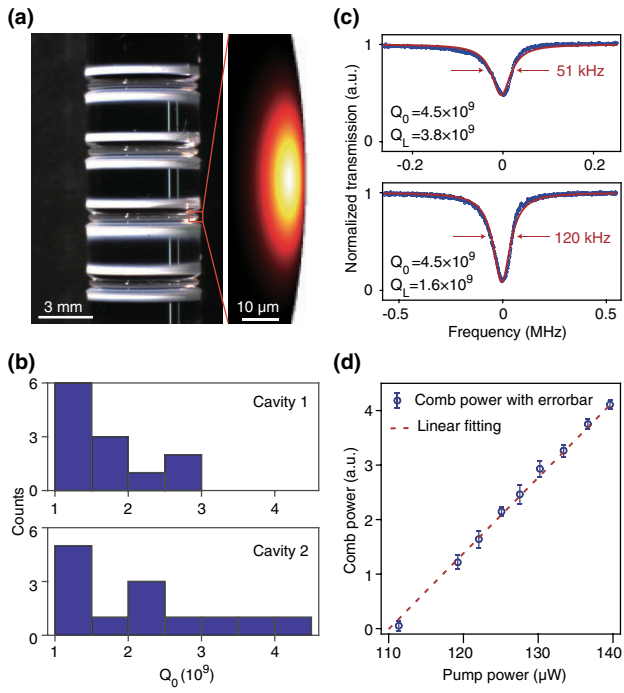
The microresonators are fabricated by irradiating CO<sub>2</sub> lasers on silica microrods that are mounted on a spindle [27]. After the geometry of the microresonators are defined, a reflow process is introduced to refine surface uniformity. In place of quartz crystals, the silica microrods are drawn from high-purity fiber preforms to reduce material imperfections and density fluctuations.

Figure 2(a) shows four silica microresonators with diameters of 6 mm, which are fabricated consecutively during an automatic process. According to the 202  $\mu\text{m}$  radius of curvature inferred from a zoom-in image, the effective mode area of the fundamental TM mode in the second microresonator is derived as 240  $\mu\text{m}^2$ . The  $Q$  factors are measured using a tunable narrow linewidth fiber laser (Koheras BASIK E15, NKT Photonics) that is coupled to the microresonator via a tapered fiber. The frequency scanning of the laser is calibrated by a Mach-Zehnder interferometer. Figure 2(b) plots the statistical diagrams of  $Q_0$  measured in two microresonators on a single microrod, where more than 10 modes exhibit intrinsic  $Q_0$  factors exceeding 1 billion. The transmission spectra of the mode with highest  $Q_0$  in the undercoupling and overcoupling regimes are showcased in Fig. 2(c). The intrinsic  $Q_0$  of 4.5 billion, to the best of our knowledge, represents the best result attained in lathe-machined silica microrods. Notably, such  $Q_0$  is sustainable in atmosphere environment for a few months. The high quality factor is expected to reduce threshold power of parametric oscillation according to the theoretical formula [8]

$$P_{\text{th}} = \frac{\pi n_0 \omega_0 A}{4\eta n_2 D_1 Q_L^2}, \quad (2)$$

with  $n_2$  the nonlinear refractive index,  $\omega_0$  the resonant frequency, and  $\eta = Q_L/Q_0$ . Experimentally, the threshold behavior is investigated by recording the power of the generated optical sidebands at different levels of pump power. As shown in Fig. 2(d), when the microresonator is overcoupled, the linear fitting is extrapolated to give a threshold power around 110  $\mu\text{W}$ , which is substantially lower than any reported values in other millimeter-sized microresonators [8,28]. We stress that sub-100  $\mu\text{W}$  threshold power is feasible by further optimizing the coupling condition.

Soliton microcombs are generated by pumping the microresonator with an amplified fiber laser based on a two-step power modulation, and long-term operation is sustained by referencing the laser frequency to certain power of the soliton [33]. The optical spectrum of the soliton is displayed in Fig. 3(a), which features a characteristic sech<sup>2</sup> spectral envelope with residual pump suppressed using a notch filter. The spurs that disrupt the spectral envelope are identified as dispersive waves due to the interaction between distinct spatial modes [20]. The microcomb is amplified and directed to a fast photodetector for microwave generation, giving rise to a monotone beatnote with high SNR at 11.4 GHz, shown in the inset of Fig. 3(a). The coherence of the SMO is characterized using a phase noise analyzer (Rodhe & Schwarz FSWP50) and typical phase noise traces are plotted in Fig. 3(b). We access the “quiet point” by monitoring the phase noise at different pump-cavity detunings until the lowest noise level is reached [12,20,21]. At this point, the phase noise of the pump laser is decoupled from the soliton repetition rate due to the balance between the Raman effect and dispersive-wave-induced spectral recoil, leading to an additional 20 dB noise reduction. The resulting phase noise reaches  $-107 \text{ dBc/Hz}$  and  $-133 \text{ dBc/Hz}$  at 1 kHz and 10 kHz offset frequencies, respectively. However, further noise reduction is not attainable in our experiment, and such a limit is speculated to result from thermal noise through a pathway mediated by the dispersive waves [21]. Other fundamental noise contributions (i.e., thermal fluctuations of the FSR and the quantum timing jitter [34]), are also plotted and apparently do not account for the noise limit. It is worth noting that shot noise



**Fig. 2.** Device property. (a) Microresonator image and mode profile. (b) Transmission spectra of soliton mode measured in the undercoupling and overcoupling regime. The intrinsic ( $Q_0$ ) and loaded ( $Q_L$ )  $Q$ -factors are extracted by fitting the Lorentzian lineshapes and transmission minima. The FWHM linewidth is measured to be 51 kHz and 120 kHz, corresponding to loaded  $Q$  factors ( $Q_L$ ) is 3.6 billion and 1.6 billion, respectively. (c) The statistics of modes with  $Q_0$  over 1 billion measured from two different devices at 1550 nm, respectively. (d) Plot of parametric oscillation power versus input power (1550 nm) showing an oscillation threshold of 110  $\mu\text{W}$ .

becomes the dominant noise source at offset frequencies beyond 30 kHz.

Figure 3(c) compares the performance of free-running microwave oscillators generated by nonlinear optics in silica microresonators [3,21,35]. Instead of the phase noise, here jitter spectral density is chosen as the figure of merit since it is irrespective of carrier frequencies. If thermal noise limit is reached, a six-fold improvement in the noise performance is anticipated in our SMO compared to other devices, as the effective mode area of fundamental modes in these silica microdisks [8,21,29] are around  $40 \mu\text{m}^2$ . Indeed, at offset frequencies below 30 kHz, the measured jitter here is around 10-dB lower than the best results attained in silica microdisks. In addition, our SMO also exhibits excellent noise performance at low offset frequencies, approaching the stability provided by a high-end electronic oscillator (Keysight PSG E8257D).

Finally, as a benchmark, the viability of using SMOs as local oscillators in data transmission systems is examined. To mitigate the temperature and coupling instability, the microresonator is encapsulated in a metallic package with the temperature stabilized by a thermoelectric cooler, as shown in the inset of Fig. 4(a). The experimental setup is depicted in Fig. 4(a), where the data stream generated by an arbitrary waveform generator is encoded onto a 10 MHz microwave through IQ modulation, and is then mixed with the carrier microwave. The output signal of the transmitter is analyzed by a vector signal analyzer to establish the constellation diagrams. To comply with 5G technology, the modulation format

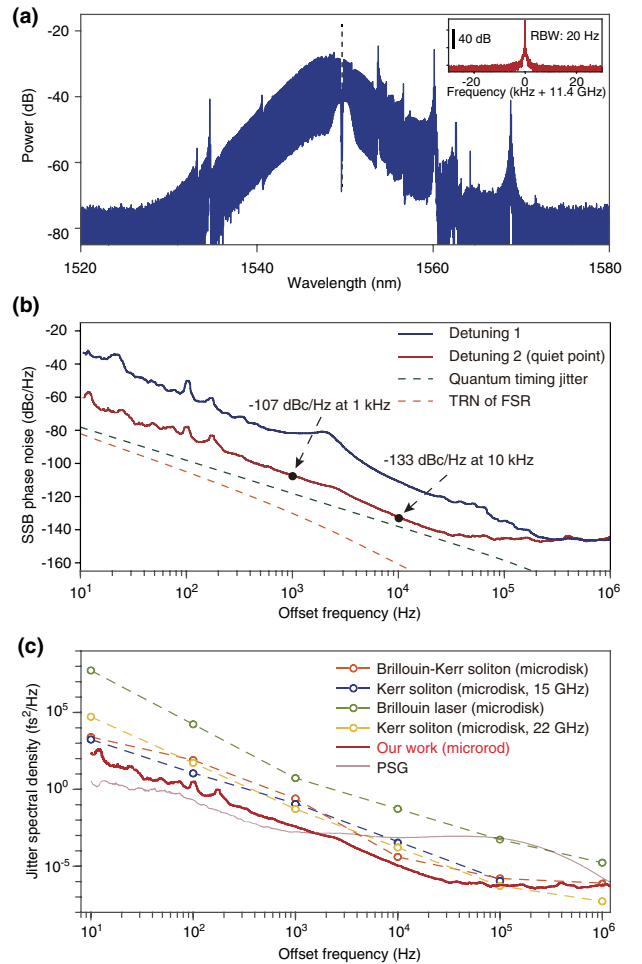


**Fig. 3.** Soliton microwave oscillator. (a) Optical spectrum of the soliton microcomb. The attenuated pump is indicated by the dashed line. Inset: Electrical spectrum showing soliton repetition rate. (b) Measured SSB phase noise at two different laser-cavity detunings. The expected quantum timing jitter and TRN of the FSR are indicated. Parameters used to calculate the results are:  $D_1/2\pi = 11.4 \text{ GHz}$ , dispersion  $D_2/2\pi = 2.1 \text{ kHz}$ ,  $Q_L = 0.7 \times 10^9$ , and  $n_2 = 2.2 \times 10^{-20} \text{ m}^2/\text{W}$ . (c) Free-running timing jitter of microwave oscillators generated using silica microresonators. Best results obtained in regular Kerr solitons [4,21], Brillouin–Kerr solitons [35], and Brillouin lasers [3] are included for comparison. The performance of an electrical PSG is also plotted.

is chosen as 256 and 1024QAM and the baud rate is 120 kHz. The constellation diagrams shown in Fig. 4(b) are reconstructed from 10 consecutive measurements with 80,000 symbols detected in total. According to the explicit separation between constellation points, the transmitter is anticipated to operate in an error-free manner. We evaluate the quality of the transmitted signal based on the averaged error vector magnitude, which are merely 1.1% and 1.26% for 256 and 1024QAM, respectively. These results highlight the capability of SMOs as low-noise local oscillators in modern communications systems.

In summary, we have demonstrated an X-band SMO in an oversized silica microresonator. By introducing fiber preforms for lathe machining, a drastic improvement of  $Q$  factors is realized to neutralize the surge of power consumption. Since thermal fluctuations are alleviated by the enlarged mode volumes and the low absorption of the high-purity fiber preforms, these SMOs feature appealing noise performance that is challenging for silica

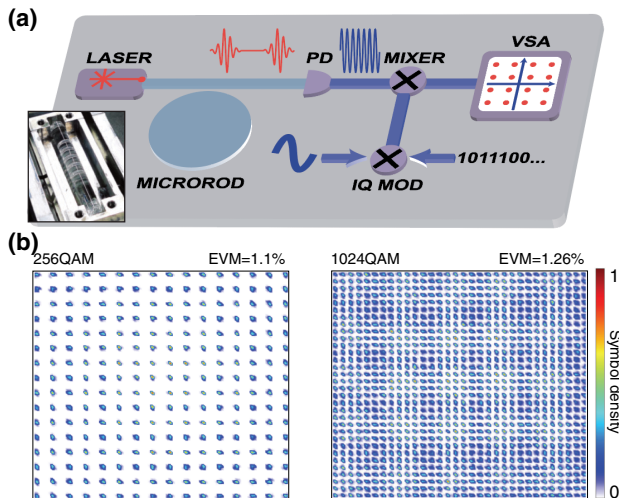


**Fig. 4.** Data transmission experiment. (a) Apparatus of the data transmitter. Inset: photo of a packaged microresonator. (b) Constellation diagrams of 256 and 1024 QAM. The normalized symbol density in the complex planes are indicated by color. The baud rate is 120 kHz.

microresonators with smaller mode volumes [3,21,35]. Applying SMOs as carrier microwave sources in high-speed data links has been tested, showing compatibility with the latest 5G technology in terms of noise performance. Our results offer a generic guideline for coherence engineering of SMOs, which should be applicable to other material platforms such as MgF<sub>2</sub> [6,7,12] and Si<sub>3</sub>N<sub>4</sub> [11,14]. While this study is focused on the free-running SMOs, recent advances in miniaturized optical atomic clocks [36] and optical frequency division technology [15] has endowed SMOs with appreciable long-term stability. Combining all these approaches would accelerate the integration of SMOs into further radar and communications systems.

**Funding.** Beijing Municipal Science & Technology Commission (Z201100004020007); Beijing Municipal Natural Science Foundation (Z210004); National Natural Science Foundation of China (11825402, 92150108, 92150301).

**Acknowledgment.** The authors thank Wen Chen, Bing Duan, and Daquan Yang from Beijing University of Posts and Telecommunications for assistance in device preparation, Qi-Tao Cao and Xing Jin from Peking University, and Qing-Xin Ji from the California Institute of Technology for helpful discussion.

**Disclosures.** The authors declare no conflicts of interest.

**Data availability.** Data underlying the results presented in this paper are available from the authors upon reasonable request.

<sup>†</sup>These authors contributed equally to this Letter.

## REFERENCES

- D. Marpaung, J. Yao, and J. Capmany, *Nat. Photonics* **13**, 80 (2019).
- L. Maleki, *Nat. Photonics* **5**, 728 (2011).
- J. Li, H. Lee, and K. J. Vahala, *Nat. Commun.* **4**, 2097 (2013).
- D. Kwon, D. Jeong, I. Jeon, H. Lee, and J. Kim, *Nat. Commun.* **13**, 381 (2022).
- Z. Lu, J.-J. Chen, W. Wang, L. Yao, Y. Wang, Y. Yu, B. Little, S. Chu, Q. Gong, W. Zhao, X. Yi, Y.-F. Xiao, and W. Zhang, *Nat. Commun.* **12**, 3179 (2021).
- T. Herr, V. Brasch, J. Jost, C. Wang, N. Kondratiev, M. Gorodetsky, and T. Kippenberg, *Nat. Photonics* **8**, 145 (2014).
- W. Liang, D. Eliyahu, V. Ilchenko, A. Savchenkov, A. Matsko, D. Seidel, and L. Maleki, *Nat. Commun.* **6**, 7957 (2015).
- X. Yi, Q.-F. Yang, K. Y. Yang, M.-G. Suh, and K. Vahala, *Optica* **2**, 1078 (2015).
- M.-G. Suh and K. Vahala, *Optica* **5**, 65 (2018).
- S. Zhang, J. M. Silver, X. Shang, L. Del Bino, N. M. Ridler, and P. Del'Haye, *Opt. Express* **27**, 35257 (2019).
- J. Liu, E. Lucas, A. S. Raja, J. He, J. Riemensberger, R. N. Wang, M. Karpov, H. Guo, R. Bouchand, and T. J. Kippenberg, *Nat. Photonics* **14**, 486 (2020).
- E. Lucas, P. Brochard, R. Bouchand, S. Schilt, T. Südmeyer, and T. J. Kippenberg, *Nat. Commun.* **11**, 374 (2020).
- B. Wang, J. S. Morgan, K. Sun, M. Jahabozorgi, Z. Yang, M. Woodson, S. Estrella, A. Beling, and X. Yi, *Light Sci. Appl.* **10**, 4 (2021).
- W. Jin, Q.-F. Yang, L. Chang, B. Shen, H. Wang, M. A. Leal, L. Wu, M. Gao, A. Feshali, M. Paniccia, K. J. Vahala, and J. E. Bowers, *Nat. Photonics* **15**, 346 (2021).
- T. Tetsumoto, T. Nagatsuma, M. E. Fermann, G. Navickaite, M. Geiselmann, and A. Rolland, *Nat. Photonics* **15**, 516 (2021).
- B. J. Eggleton, C. G. Poulton, P. T. Rakich, M. Steel, and G. Bahl, *Nat. Photonics* **13**, 664 (2019).
- D.-G. Kim, S. Han, J. Hwang, I. H. Do, D. Jeong, J.-H. Lim, Y.-H. Lee, M. Choi, Y.-H. Lee, D.-Y. Choi, and H. Lee, *Nat. Commun.* **11**, 5933 (2020).
- K. Y. Yang, D. Y. Oh, S. H. Lee, Q.-F. Yang, X. Yi, B. Shen, H. Wang, and K. Vahala, *Nat. Photonics* **12**, 297 (2018).
- J.-W. Shi, C.-B. Huang, and C.-L. Pan, *NPG Asia Mater.* **3**, 41 (2011).
- X. Yi, Q.-F. Yang, X. Zhang, K. Y. Yang, X. Li, and K. Vahala, *Nat. Commun.* **8**, 14869 (2017).
- Q.-F. Yang, Q.-X. Ji, L. Wu, B. Shen, H. Wang, C. Bao, Z. Yuan, and K. Vahala, *Nat. Commun.* **12**, 1442 (2021).
- T. E. Drake, J. R. Stone, T. C. Briles, and S. B. Papp, *Nat. Photonics* **14**, 480 (2020).
- H. Lee, M.-G. Suh, T. Chen, J. Li, S. A. Diddams, and K. J. Vahala, *Nat. Commun.* **4**, 2468 (2013).
- N. Kondratiev and M. Gorodetsky, *Phys. Lett. A* **382**, 2265 (2018).
- G. Huang, E. Lucas, J. Liu, A. S. Raja, G. Lihachev, M. L. Gorodetsky, N. J. Engelsen, and T. J. Kippenberg, *Phys. Rev. A* **99**, 061801 (2019).
- B. Li, W. Jin, L. Wu, L. Chang, H. Wang, B. Shen, Z. Yuan, A. Feshali, M. Paniccia, K. J. Vahala, and J. E. Bowers, *Opt. Lett.* **46**, 5201 (2021).
- P. Del'Haye, S. A. Diddams, and S. B. Papp, *Appl. Phys. Lett.* **102**, 221119 (2013).
- L. Wu, H. Wang, Q. Yang, Q.-X. Ji, B. Shen, C. Bao, M. Gao, and K. Vahala, *Opt. Lett.* **45**, 5129 (2020).
- H. Lee, T. Chen, J. Li, K. Y. Yang, S. Jeon, O. Painter, and K. J. Vahala, *Nat. Photonics* **6**, 369 (2012).
- I. S. Grudinin and N. Yu, *Optica* **2**, 221 (2015).
- D. Armani, T. Kippenberg, S. Spillane, and K. Vahala, *Nature* **421**, 925 (2003).
- M. L. Gorodetsky and I. S. Grudinin, *J. Opt. Soc. Am. B* **21**, 697 (2004).
- X. Yi, Q.-F. Yang, K. Youl, and K. Vahala, *Opt. Lett.* **41**, 2037 (2016).
- A. B. Matsko and L. Maleki, *Opt. Express* **21**, 28862 (2013).
- Y. Bai, M. Zhang, Q. Shi, S. Ding, Y. Qin, Z. Xie, X. Jiang, and M. Xiao, *Phys. Rev. Lett.* **126**, 063901 (2021).
- Z. L. Newman, *Optica* **6**, 680 (2019).